








Step-flow growth in homoepitaxy of β -Ga₂O₃ (100)—The influence of the miscut direction and faceting

Cite as: APL Mater. 7, 022515 (2019); <https://doi.org/10.1063/1.5054943>

Submitted: 05 September 2018 . Accepted: 03 November 2018 . Published Online: 18 December 2018

R. Schewski , K. Lion , A. Fiedler, C. Wouters , A. Popp, S. V. Levchenko, T. Schulz , M. Schmidbauer, S. Bin Anooz, R. Grüneberg, Z. Galazka , G. Wagner, K. Irmischer , M. Scheffler, C. Draxl, and M. Albrecht 



View Online



Export Citation



CrossMark

ARTICLES YOU MAY BE INTERESTED IN

Faceting and metal-exchange catalysis in (010) β -Ga₂O₃ thin films homoepitaxially grown by plasma-assisted molecular beam epitaxy

APL Materials 7, 022511 (2019); <https://doi.org/10.1063/1.5054386>

Tin-assisted heteroepitaxial PLD-growth of κ -Ga₂O₃ thin films with high crystalline quality

APL Materials 7, 022516 (2019); <https://doi.org/10.1063/1.5054378>

MOCVD grown epitaxial β -Ga₂O₃ thin film with an electron mobility of 176 cm²/V s at room temperature

APL Materials 7, 022506 (2019); <https://doi.org/10.1063/1.5058059>



Measure Ready
M91 FastHall™ Controller

A revolutionary new instrument
for complete Hall analysis

 Lake Shore
CRYOTRONICS

Step-flow growth in homoepitaxy of β -Ga₂O₃ (100)—The influence of the miscut direction and faceting

Cite as: APL Mater. 7, 022515 (2019); doi: 10.1063/1.5054943
Submitted: 5 September 2018 • Accepted: 3 November 2018 •
Published Online: 18 December 2018



R. Schewski,¹  K. Lion,²  A. Fiedler,¹  C. Wouters,¹  A. Popp,¹  S. V. Levchenko,^{3,4}  T. Schulz,¹ 
M. Schmidbauer,¹  S. Bin Anooz,¹  R. Grüneberg,¹  Z. Galazka,¹  G. Wagner,¹  K. Irmischer,¹ 
M. Scheffler,³  C. Draxl,²  and M. Albrecht¹ 

AFFILIATIONS

¹Leibniz-Institut für Kristallzüchtung, Max-Born-Straße 2, 12489 Berlin, Germany

²Humboldt-Universität zu Berlin, Institut für Physik und IRIS, Zum Großen Windkanal 6, D-12489 Berlin, Germany

³Fritz-Haber-Institut der Max-Planck-Gesellschaft, Theory Department, Faradayweg 4-6, 14195 Berlin, Germany

⁴Skolkovo Institute of Science and Technology, Skolkovo Innovation Center, 3 Nobel Street, 143026 Moscow, Russia

ABSTRACT

We present a systematic study on the influence of the miscut orientation on structural and electronic properties in the homoepitaxial growth on off-oriented β -Ga₂O₃ (100) substrates by metalorganic chemical vapour phase epitaxy. Layers grown on (100) substrates with 6° miscut toward the [00 $\bar{1}$] direction show high electron mobilities of about 90 cm² V⁻¹ s⁻¹ at electron concentrations in the range of 1–2 × 10¹⁸ cm⁻³, while layers grown under identical conditions but with 6° miscut toward the [001] direction exhibit low electron mobilities of around 10 cm² V⁻¹ s⁻¹. By using high-resolution scanning transmission electron microscopy and atomic force microscopy, we find significant differences in the surface morphologies of the substrates after annealing and of the layers in dependence on their miscut direction. While substrates with miscuts toward [00 $\bar{1}$] exhibit monolayer steps terminated by ($\bar{2}$ 01) facets, mainly bilayer steps are found for miscuts toward [001]. Epitaxial growth on both substrates occurs in step-flow mode. However, while layers on substrates with a miscut toward [00 $\bar{1}$] are free of structural defects, those on substrates with a miscut toward [001] are completely twinned with respect to the substrate and show stacking mismatch boundaries. This twinning is promoted at step edges by transformation of the (001)-B facets into ($\bar{2}$ 01) facets. Density functional theory calculations of stoichiometric low index surfaces show that the ($\bar{2}$ 01) facet has the lowest surface energy following the (100) surface. We conclude that facet transformation at the step edges is driven by surface energy minimization for the two kinds of crystallographically inequivalent miscut orientations in the monoclinic lattice of β -Ga₂O₃.

© 2018 Author(s). All article content, except where otherwise noted, is licensed under a Creative Commons Attribution (CC BY) license (<http://creativecommons.org/licenses/by/4.0/>). <https://doi.org/10.1063/1.5054943>

β -Ga₂O₃ has recently gained renewed scientific interest as a wide bandgap oxide semiconductor. With a bandgap of about 4.8 eV¹ and an estimated break down electrical field of 8 MV cm⁻¹, β -Ga₂O₃ is a promising material for power electronic and optoelectronic applications.²⁻⁵ In contrast to other wide bandgap semiconductors (e.g., SiC and GaN), β -Ga₂O₃ has the advantage that bulk single crystals with high structural perfection can be grown cost-effectively from the melt.⁶⁻⁹ Epitaxial growth on native substrates is therefore the natural choice to obtain device-grade layers. In the last

years, impressive results on homoepitaxial growth have been achieved by different growth techniques [e.g., metalorganic vapor phase epitaxy (MOVPE),^{5,10-12} molecular beam epitaxy (MBE),¹³⁻¹⁵ and halide vapor phase epitaxy (HVPE)]^{16,17} on a variety of possible substrate orientations [such as (100), (010), (001), and ($\bar{2}$ 01)].^{3,4,18} The substrate orientation has been chosen in terms of the achievable growth rate for the respective growth method and the available substrate size or a combination thereof: in MBE, e.g., the growth rate on (010)-oriented substrates is an order of magnitude higher than

that on (100),¹⁵ while it is substantially independent on substrate orientation in MOVPE.¹² Previously we showed¹⁰ that homoepitaxial growth on the (100) plane without or with a small substrate miscut is characterized by a 2D island nucleation growth mode. In that case, double positioning of Ga adatoms induces the formation of twin lamellae that impair the electrical transport properties of the films.^{19,20} By introducing an appropriate miscut of 6°, the terrace width becomes small enough and comparable to the diffusion length of adatoms on the surface which in turn enables stable step-flow growth on the (100) plane of β -Ga₂O₃ leading to superior crystalline and thus electrical properties. Interestingly, it was shown that in the case of heteroepitaxial growth on sapphire the introduction of a desired miscut leads to a single crystalline layer with improved electrical properties.²¹ Up to now, the desired step flow growth during homoepitaxial growth has exclusively been shown on (100) surfaces,^{13,19,14} while the growth on all other surfaces results either in faceted surfaces²² or a three-dimensional surface structure, not reproducing the initial monoatomic stepped surface structure of the substrate.

In this paper, we combine transmission electron microscopy (TEM), electrical characterization, and first principle calculations to study homoepitaxial growth of β -Ga₂O₃ layers by MOVPE on (100) native substrates. We show that due to the monoclinic symmetry miscuts toward [001] and [00 $\bar{1}$] are not equivalent. While annealed substrate surfaces with miscuts toward [00 $\bar{1}$] show monolayer steps with heights of half a unit cell and terminated by (201) facets, their counterparts exhibit a mixture of bilayer steps with the height of a full unit cell as well as monolayer steps. Epitaxial growth on (100) substrates with a miscut toward [00 $\bar{1}$] results in epitaxial layers of high crystalline quality, while growth on (100) substrates with the miscut toward [001] results in a complete twinning of the layer with respect to the substrate. The latter causes stacking mismatch boundaries that are electrically active as compensation and scattering centers reducing the concentration of charge carriers and their mobility. According to our first principle calculations, the twinning of the layer is explained by minimization of the surface energy. In contrast to the general belief that the cleavage planes (100) and (001) have the lowest surface energy, we show that (201) surfaces are substantially lower in energy than (001). Hall effect measurements of series of samples grown on substrates with miscut angles of 6° toward [00 $\bar{1}$] and [001] show that those grown with the miscut toward [00 $\bar{1}$] have reproducibly high mobilities that are in the range of the best values published in the literature,^{15,23,24} while those grown with miscuts toward [001] have extremely low values.

β -Ga₂O₃ single crystals are grown by the Czochralski method.^{6,8,25} (100) oriented substrates with a size of 5 × 5 × 0.5 and 10 × 10 × 0.5 mm³ are prepared from such boules with a miscut of +6° toward the [001] and [00 $\bar{1}$] directions, respectively. The substrates are electrically insulating due to intentional Mg doping. The square-shaped substrates had their edges parallel to [010] (**b**-direction) and [001] (**c**-direction), respectively, and the sample surface coincided

with the predefined (100) miscut orientation. As-fabricated substrates show smooth surfaces with a roughness of 0.17 nm. No surface steps are observable independent of the desired miscut orientation due to a damaged layer, created by the polishing process. After cleaning with acetone and isopropanol in an ultrasonic bath, the substrates are etched in phosphoric acid at 140 °C for 15 min to remove the polishing damage. Afterwards the substrates are annealed in oxygen atmosphere at 900 °C for 60 min to achieve a well-defined, stepped surface. Prior to growth, a dip in hydrofluoric acid for 5 min passivates the epi-ready surface. The β -Ga₂O₃ layers are grown in a vertical showerhead low pressure MOVPE system (Structured Materials Industries, Inc., USA) equipped with a rotating 3" susceptor. Triethyl-gallium (TEGa) and pure oxygen are used as gallium precursor and oxygen source, respectively. Silicon, which is a shallow donor in β -Ga₂O₃, is used as the dopant. Tetraethyl-orthosilicate (TEOS) is used as silicon precursor. The temperature of TEGa and TEOS bubblers is kept at 20 °C and 5 °C, respectively. The TEGa and O₂ molar flows are kept at 6.1 × 10⁻⁶ and 2.2 × 10⁻² mol/min, while that of TEOS is set at 2 × 10⁻¹⁰ mol/min. High purity Ar, with a main flow rate of 1500 SCCM, is used as a carrier gas. The growth process is performed at 825 °C and 5 mbar chamber pressure since these parameters were found to result in layers with best structural and electrical properties.¹² The resulting growth rate is 2 nm/min, and a free electron concentration of 1–2 × 10¹⁸ cm⁻³ is obtained. The layer thickness is measured by spectral ellipsometry (MM16, Horiba Jobin Yvon) on β -Ga₂O₃ layers grown simultaneously on sapphire substrates. This was possible since we had crosschecked by secondary ion mass spectroscopy (SIMS) and TEM that the layer thickness on both substrates is the same within 2% variation. The surface morphology is determined by AFM measurements (Bruker, dimension icon).

Electrical characterization of the layers on insulating substrates is performed by resistivity and Hall effect measurements at room temperature using a commercial setup (Lake Shore HMS 7504) and contacting the samples in van der Pauw configuration. Point-like ohmic contacts are prepared by applying InGa eutectic in the four corners of the samples.

Transmission and scanning transmission electron microscopy (TEM and STEM) measurements are performed with an FEI Titan 80-300 operated at an acceleration voltage of 300 kV. The microscope is equipped with an aberration corrector for the objective lens and a high brightness field emission gun (X-FEG) as an electron source. STEM imaging is performed with a focused, convergent beam with a semi-convergence angle of $\alpha = 9.0$ mrad, using a high angle annular dark-field (HAADF) detector (Fisheye model 3000). TEM samples are prepared by face-to-face gluing, followed by mechanical polishing to a thickness of about 10 μ m. Electron transparency is achieved by ion beam milling (Gatan PIPS), with an incident angle of the ion beams of 4° and an acceleration voltage of 3.5 kV under liquid nitrogen cooling, and finally by a stepwise reduction of the acceleration voltage down to 0.2 kV.

First-principles total energy calculations are performed in the framework of density-functional theory (DFT), employing a numerical atom-centered orbital basis set, as implemented in the full-potential all-electron code FHI-aims.^{26,27} A k -point sampling of $6 \times 14 \times 12$ is used to calculate the ground state of the conventional bulk cell. The basis set and numerical grids are defined by the “tight” settings for both the gallium and oxygen atoms.²⁶ The unit cell and surface slabs of β -Ga₂O₃ are relaxed without constraints using the PBEsol functional²⁸ until the forces acting on the atoms are smaller than 10 meV/Å. For these geometries, calculations with the HSE06 hybrid functional²⁹ are performed. The difference in optimized geometries using PBEsol or HSE06 is found to be negligible. In the HSE06 calculations, the basis set and numerical grids for gallium are defined by the “intermediate” settings. For the (100) and (201) surfaces, the surface energies differ by less than 0.05 J/m² when using “tight” settings. Using the open-source python library pymatgen,^{30–32} non-polar and stoichiometric slabs are created from the relaxed bulk structure that preserve the symmetry of the bulk cell. Surface slabs are modelled as supercells including a vacuum of 30 Å. The number of layers within each slab is considered as converged when the surface energies differ by less than 0.01 J/m².

Figures 1(a) and 1(b) show AFM images of annealed (100) substrate surfaces with a miscut angle of 6° toward the [001] and [001] directions, respectively, prior to homoepitaxial growth. Substrates oriented toward the [001] direction exhibit

a regular stepped surface with terrace widths of about 5 nm. By contrast, substrates with a miscut direction toward the [001] direction are more irregularly stepped. While the steps are still well aligned along [010] directions, the most remarkable finding is that the terrace widths are significantly wider than on the substrates with the miscut toward [001] despite the same miscut angle. Cross-sectional STEM-HAADF images recorded along the [010] projection direction, i.e., along the direction of the surface steps, shown as insets in Figs. 1(a) and 1(b) resolve the atomistic origin of this discrepancy. The steps at the surface of substrates with a miscut toward [001] are monolayer as well as bilayer steps; i.e., they have the height of a full unit cell, while the substrate with the surface miscut toward [001] shows exclusively mono-layer steps of half a unit cell height.

Figures 1(c) and 1(d) show corresponding AFM images of the surface after growth of a 200 nm thick layer. For growth on substrates with a step-down direction toward [001], the surface morphology mimics the step structure of the substrate prior to growth, i.e., it is formed of regularly spaced surface steps aligned along [010], indicating a perfect step-flow growth mode. By contrast, growth on a substrate with a step-down direction toward the [001] results in rough homoepitaxial layers, characterized by three-dimensional islands, which are elongated toward the b -direction, and show steep edges, indicating step bunching.

Figure 2 shows electron mobilities as a function of the charge carrier concentration for homoepitaxial layers of a series of samples grown pairwise in the same run on substrates with a 6° miscut toward the [001] and [001] directions, respectively. Layers grown on substrates with the miscut toward the [001] direction show bulk-like electron Hall mobilities of $80 \pm 15 \text{ cm}^2 \text{ V}^{-1} \text{ s}^{-1}$ for the average free electron concentrations of $(1.6 \pm 0.3) \times 10^{18} \text{ cm}^{-3}$. By contrast, layers grown on substrates with the miscut toward the [001] direction exhibit much lower electron mobilities of $8 \pm 1 \text{ cm}^2 \text{ V}^{-1} \text{ s}^{-1}$, which is additionally accompanied by a lower free electron concentration. Such low Hall mobilities are typical for

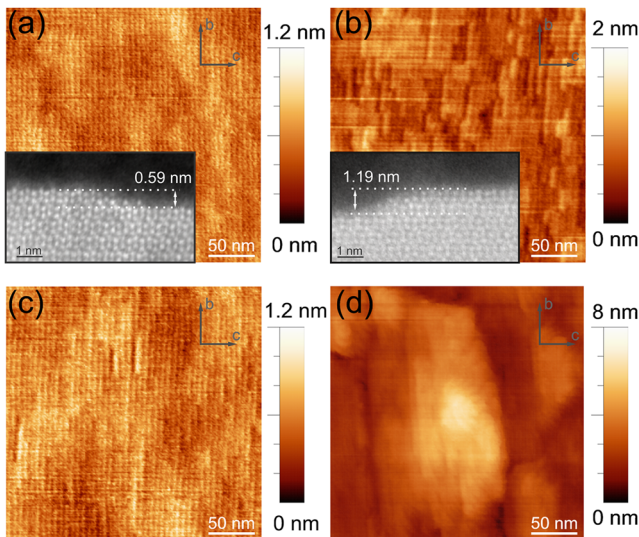


FIG. 1. AFM images of annealed β -Ga₂O₃ (100) substrates with a miscut of 6° toward (a) the [001] and (b) the [001] directions. The insets show atomically resolved cross-sectional STEM images (Ga atoms appear as bright dots) recorded along the [010] projection direction, of the layer grown on the substrates shown in (a) and (b), respectively. The step in (a) is a monolayer step of half a unit cell thickness; the step in (b) is a bilayer step of a unit cell height; [(c) and (d)] AFM images of the surface of the layer grown on substrates shown in (a) and (b), respectively. Step-flow growth is observed in (c), and three-dimensional growth is observed in (d).

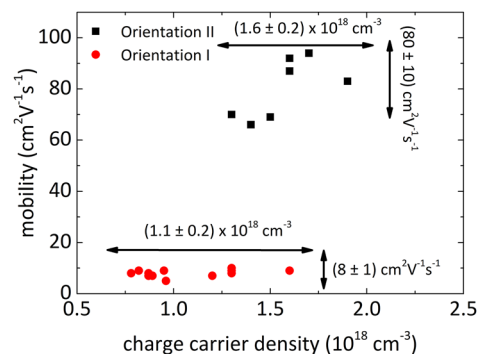


FIG. 2. Electron Hall mobility as a function of the electron Hall concentration at room temperature for β -Ga₂O₃ layers homoepitaxially grown by MOVPE on (100) oriented substrates with a predefined miscut of 6°, either along [001] (red dots) or [001] (black squares).

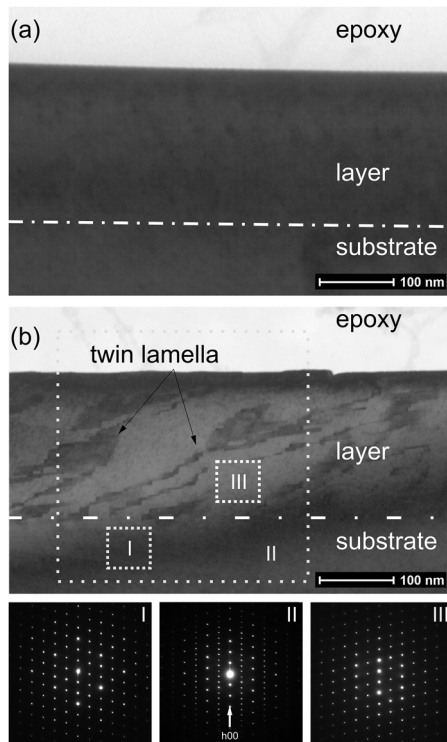


FIG. 3. (a) Cross-sectional TEM bright field image of a layer grown on a substrate with a miscut direction toward $[00\bar{1}]$. (b) Cross-sectional TEM bright field image of a layer grown on a substrate with a miscut direction toward $[001]$. The white dashed-dotted lines correspond to the interface between the layer and the substrate. The selected area diffraction pattern is taken from I, II, and III and corresponds to the highlighted areas marked in (b).

layers grown on (100) oriented substrates without an intentional miscut, containing a large amount of incoherent twin boundaries.²⁰

Figures 3(a) and 3(b) show cross-sectional TEM bright field images of the layers grown on substrates with miscuts toward the $[00\bar{1}]$ and $[001]$ directions, respectively. In the case of a miscut toward $[00\bar{1}]$ [Fig. 3(a)], the layer is hardly distinguishable from the substrate, i.e., it is free of extended defects, as expected for layers grown in step-flow mode. In contrast, for the miscut toward $[001]$, the interface between the substrate and the layer is clearly visible, characterized by extended defects with a spacing of 50–100 nm that climb through the layer. As reported in a previous paper, these are stacking mismatch boundaries, formed between two adjacent regions which are shifted by half of a unit cell along the $[100]$ direction against each other.¹⁹ These stacking mismatch boundaries are electrically active as compensation and scattering centers reducing the concentration of charge carriers and their mobility, as described by Fiedler *et al.*²⁰ An even more striking result is obtained by analyzing selected area electron diffraction patterns taken from the layer, the substrate, and both together. Figure 3(b–I) shows the

diffraction pattern of the undisturbed substrate. The diffraction pattern of the layer in Fig. 3(b–III) is, compared to the substrate, mirrored at the (100) plane; i.e., the complete layer is twinned with respect to the substrate. In the selected area diffraction pattern taken from the layer and substrate, the twin relation of the layer is seen by the superposition of the g_{h00} spots originating from the substrate and the film [Fig. 3(b–II)]. The change in the orientation of the layer with respect to the substrate is characterized by a $c/2$ glide reflection as described in our previous work.^{10,19}

A representative image of the atomic structure of the interface between the substrate and the twinned layer is shown in Fig. 4(a). The STEM-HAADF image was taken along the $[010]$ zone axis of the monoclinic lattice. In this projection, the atomic column contrast arises mainly from the gallium columns because of the much higher atomic number of gallium ($Z = 31$) compared to oxygen ($Z = 8$). The interface between the layer and the substrate is indicated by the red dotted line. A stick and ball model derived from the STEM-HAADF image is shown in Fig. 4(b). Three important findings should be highlighted here. First, the stacking order of the atoms reverses to the twinned orientation at the interface between the layer and the substrate. Second, the step edge has the height of a full unit cell, confirming our finding of bilayer steps at the substrate surface reported in Fig. 1(b). It should be noted that bilayer steps are clearly dominating the interface between the

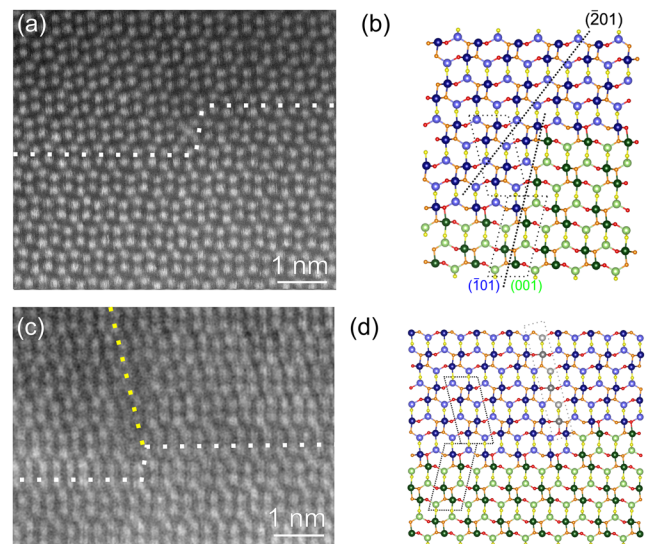


FIG. 4. Interface between the layer and the substrate of a layer grown on substrates with a miscut toward $[001]$. (a) Atomically resolved STEM-HAADF image of the interface shown in Fig. 3(b). The dotted line indicates the interface between the layer and the substrate, containing a bilayer step. The layer is twinned with respect to the substrate. (b) Atomic model of the layer. The $(\bar{2}01)$ facet that nucleates on the (001) -B facet is indicated. (c) Atomically resolved STEM-HAADF image of the interface region between the layer and the substrate showing a monolayer step and the emerging stacking mismatch boundary. (d) Stick and ball model of the step and emerging defect shown in (c). Gallium columns are either blue, green, or gray, while oxygen columns are red, orange, and yellow, respectively.

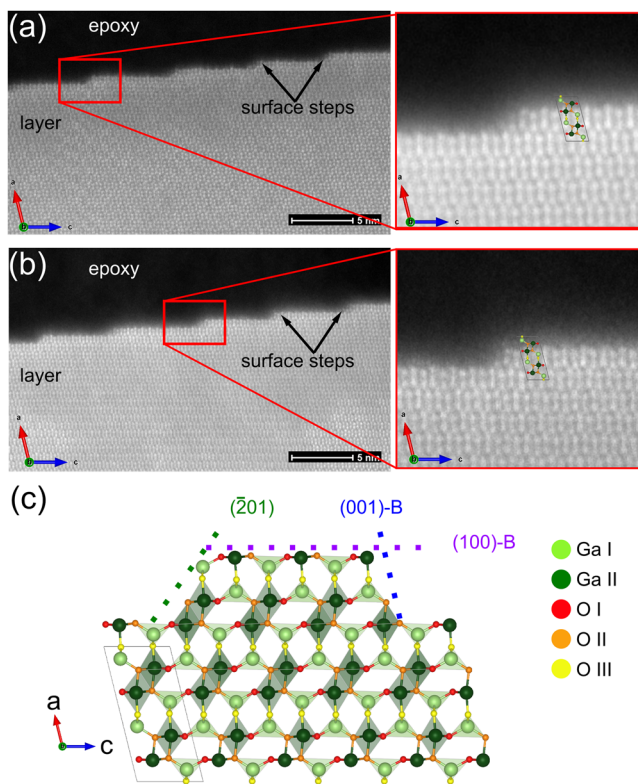


FIG. 5. [(a) and (b)] STEM HAADF images of the surface of a layer grown on a substrate with $[00\bar{1}]$ and $[001]$ step down directions, respectively. The magnified regions show the typical step morphology in the $[010]$ projection. (c) shows a stick and ball model of the observed step structure. Bright and dark green balls correspond to tetrahedral and octahedral bound Ga columns, respectively. Red, orange, and yellow balls correspond to the 3 different oxygen positions O(I), O(II), and O(III), respectively.

substrates and the epitaxial layer, while mono-atomic steps are also found by high-resolution STEM imaging, however, with much higher average spacing of 50–100 nm. Stacking mismatch boundaries (as described in our previous publication¹⁹) form at these interface steps having a thickness of half a unit cell in the a -direction, as shown in Fig. 4(c). Figure 4(d)

shows a stick and ball model of the observed monolayer step. The positions of the Ga atoms forming the stacking mismatch boundary are highlighted as gray balls. Third, the side-facet of the bi-layer height surface step edge is a $(\bar{2}01)$ surface in the twinned layer, while the step edge corresponds to a (001) -B surface of the substrate, as described by Bermudez.³³

Figures 5(a) and 5(b) show cross-sectional high-resolution STEM-HAADF images of the surface of the layers grown on substrates with a $[00\bar{1}]$ and a $[001]$ miscut direction, respectively, along the $[010]$ projection direction. For both miscut orientations, we found a periodic arrangement of surface steps that have a height of half a unit cell ($a/2 = 059$ nm) and an average spacing of 5–6 nm, which is in good accordance with the miscut angle. Note that the substrate surface with the miscut toward $[00\bar{1}]$ showed bilayer steps. From magnified images of the step edge, we allocate the exact position of the octahedral and tetrahedral coordinated gallium sites as described above and shown in the stick and ball models of the β - Ga_2O_3 unit cell superimposed with the images. From such analysis, we find that in both cases, the as-grown surface is a (100) -B surface according to the terminology of Bermudez, which is the (100) surface termination with the lowest energy.³³ More importantly, we confirm that, despite the initially different miscut direction, the surface of the grown layer exhibit an identical step down direction [Fig. 5(b)] along $[00\bar{1}]$. Hence the miscut orientation at the surface of the layer grown on the substrate with miscut toward $[001]$ is converted to that of the layer grown on a substrate with a miscut toward $[00\bar{1}]$. This is in excellent agreement with our finding by TEM that the complete layer is twinned with respect to the substrate. According to first principle calculations by Bermudez, the (001) surface, a cleavage plane, corresponds to the surface with the second-lowest surface energy after the (100) surface.³³ It is therefore expected that the step edges should be terminated by (001) facets. Instead, our TEM data show that step edges at the surface are bound by $(\bar{2}01)$ facets. Figure 5(c) shows a stick and ball model of the various surface facets, i.e., $(\bar{2}01)$, (001) -B, and (100) -B, which are relevant for our discussion.

Since the surface energy of $(\bar{2}01)$ facets has not been calculated so far, we performed DFT PBEsol and HSE06 calculations of the energies for a variety of surfaces, including $(\bar{2}01)$. Figure 6(a) shows the calculated surface energies. The surface

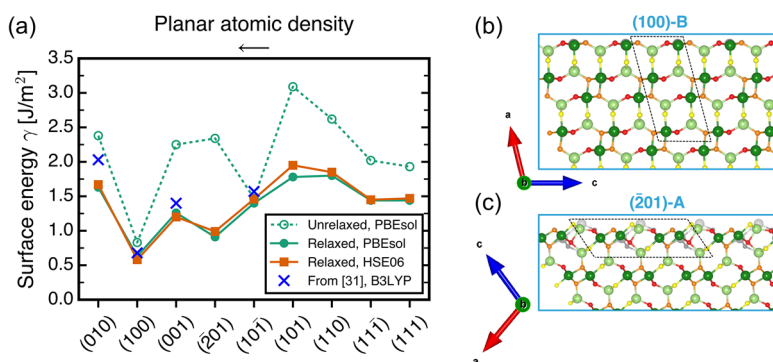


FIG. 6. (a) Calculated energies of different β - Ga_2O_3 surfaces. The surface terminations are ordered from left to right on the x-axis according to decreasing planar atomic density. If more than one surface termination is available for a given Miller plane, only the termination with the lowest surface energy is shown. [(b) and (c)] Side view of the two surface terminations with the lowest surface energies. Two terminations (A and B) can be found for both the (100) and the $(\bar{2}01)$ surfaces. Here, we only show the most stable termination for both Miller planes. The relaxed slab (colored spheres) is superimposed with the unrelaxed slab (light gray spheres). The color-code for gallium and oxygen atoms is the same as in Fig. 5. The dashed parallelograms indicate the surface unit cell.

energy γ for a clean, symmetric, and stoichiometric surface slab is defined as

$$\gamma = \frac{1}{2A}(E_{\text{slab}} - Ne_{\text{bulk}}). \quad (1)$$

Here, A is the surface area, E_{slab} is the total energy of the slab supercell, e_{bulk} is the total energy of the bulk cell per atom, and N is the number of atoms in the surface slab. The factor $\frac{1}{2}$ accounts for the two identical surfaces in the slab. E_{slab} was calculated for the relaxed as well as the unrelaxed structures. In all cases, the surface energy is lowered upon fully relaxing the surface slabs. This reduction, however, differs significantly between the different surfaces: while the PBESol surface energy of the (100)-B surface is only reduced by 0.2 J/m^2 (32% reduction in energy), the biggest reduction can be found for the $(\bar{2}01)$ -A surface with 1.4 J/m^2 (257%). Side views of both surfaces are shown in Figs. 6(b) and 6(c), respectively. The relaxation of the $(\bar{2}01)$ -A surface is complex and leads to a significant flattening of the surface. In agreement with previously published results,³³ the most stable surface termination is (100)-B that corresponds to the cleavage plane of the bulk cell. The second most stable termination is $(\bar{2}01)$ -A. These results support the experimental findings that $(\bar{2}01)$ facets are more prevalent than (001) facets. The results show little dependence on the employed exchange-correlation functional as evident from Fig. 6(a). We want to emphasize that all created slabs are stoichiometric. As a result, the surface energy is independent of the individual chemical potentials under the conditions when the bulk $\beta\text{-Ga}_2\text{O}_3$ is thermodynamically stable.²⁷ We do not take surface adsorption, surface defects, or surface reconstructions into account. All these phenomena play a role in experiments and can influence the stability of individual surfaces. The influence of these effects will be investigated in a forthcoming theoretical study.

Based on our experimental results and our findings on surface energies from first principle calculations and considering the symmetry of the monoclinic lattice, we may draw the following simple model to explain our experimental findings. In the case of epitaxial growth on substrates with the miscut toward the $[00\bar{1}]$ direction, step edges form $(\bar{2}01)$ facets that have significantly lower surface energies than the (001) surface. If the substrate miscut is toward $[001]$, there is no symmetry equivalent surface that would correspond to the $(\bar{2}01)$ facet. Since in this orientation all other considered surfaces are higher in energy, we would expect (001) facets to form. However as shown in Fig. 3(b), nucleation of a twinned $(\bar{2}01)$ terminated nucleus on the (001)-B facet is found experimentally. This converts the crystal structure into the twinned orientation directly at the step edge and thus significantly reduces the surface energy. The study of a number of samples grown under different growth conditions (e.g., growth temperature and precursor fluxes) and of various steps at the interface between the twinned layers confirms our findings. At the moment, the detailed mechanism for the nucleation as well as the detailed atomic structure of the twinned (001) facet is not fully understood since it would require a study on the oxygen atomic positions. While in our previous work

formation of a twin lamella¹⁹ was statistical and caused by random nucleation of 2D islands on surface terraces, we find here twinned step-flow growth. This twinned step-flow growth suppresses the random nucleation of two-dimensional islands on terraces, which is corroborated by the fact that the volume of the layer is completely free of the twin lamella. The spacing of stacking mismatch boundaries is equal to the spacing of monolayer steps between the substrate and the layer. This distance is higher than in the case observed in AFM and STEM measurements of the annealed surface, before growth. This increase in the distance between the monolayer steps on the surface is a result step bunching, decreasing the amount of high energetic stacking mismatch boundaries. While twinning at step edges has not been observed in any other material system, to the best of our knowledge, some of our findings, i.e., the transition from monolayer steps to bilayer steps with the change in the miscut direction from $[00\bar{1}]$ to $[001]$, resemble the findings on Si or GaAs.^{34,35} In the case of Si, for example, the appearance of bilayer steps depends on the miscut angle and the miscut direction.³³ In this case, surface reconstructions play the crucial role, which is not expected for stoichiometric (100)-B surfaces in $\beta\text{-Ga}_2\text{O}_3$. More experimental and theoretical studies are needed to understand the surfaces and steps of monoclinic $\beta\text{-Ga}_2\text{O}_3$. Our finding that (001) surfaces may easily transform into a low energetic $(\bar{2}01)$ surface may also shed some light on recent findings on low mobilities in Ge doped layers grown on (001) surfaces.³⁶ While these authors found perfectly stepped surfaces before layer growth, the surface is rough after growth and mobilities are in the range of $20 \text{ cm}^2 \text{ V}^{-1} \text{ s}^{-1}$. This could be assigned to the formation of misoriented domains that cause structural defects and thus reduce carrier mobility.

In summary, we have shown that homoepitaxial growth of monoclinic $\beta\text{-Ga}_2\text{O}_3$ have some unexpected peculiarities that need to be considered to exploit the full potential of this material system. We showed that the orientation of the miscut toward $[001]$ and $[00\bar{1}]$ of (100) oriented wafers plays a crucial role for the surface and structural quality of epitaxial layers. While predominantly bilayer steps are found for miscut toward $[001]$, monolayer steps are present for the miscut toward $[00\bar{1}]$ despite the same miscut angle of 6° . On substrates with miscuts toward the $[001]$ direction, our STEM investigations show that the formation of $(\bar{2}01)$ facets convert the growing layer by twinning at the (001)-B step facet into a completely twinned layer. Here, growth still occurs in the step-flow mode. First principle calculations show that the $(\bar{2}01)$ facet has the lowest free surface energy following the (100) surface. While it is commonly believed that the cleavage planes (100) and (001) should have the lowest surface free energies, the $(\bar{2}01)$ exhibits a huge lattice relaxation due to the shift of the tetrahedrally coordinated surface atoms into the surface. The presence of monolayer steps in these layers (grown on substrates with the miscut toward $[001]$) causes stacking mismatch boundaries that hamper electrical transport. In a series of experiments, we could show that reproducible electrical properties with the state-of-the-art mobilities can exclusively be obtained on (100) surfaces with

the 6° miscut toward the [001] direction. Our study emphasizes that understanding growth surfaces of β -Ga₂O₃ is crucial for improving the structural quality of epitaxial layers on differently oriented substrates and for optimizing the electronic properties.

This work was partly financed from the funds of the German Research Foundation (DFG) (Grant No. GA 2057/2-1) and by GraFOx, a Leibniz-Science Campus partially funded by the Leibniz Association, Germany. We thank Toni Markurt for carefully reading the manuscript.

REFERENCES

- ¹C. Janowitz, V. Scherer, M. Mohamed, A. Krapf, H. Dwelk, R. Manzke, Z. Galazka, R. Uecker, K. Irmscher, R. Fornari, M. Michling, D. Schmeißer, J. R. Weber, J. B. Varley, and C. G. Van de Walle, *New J. Phys.* **13**, 085014 (2011).
- ²M. Zhong, Z. Wei, X. Meng, F. Wu, and J. Li, *J. Alloys Compd.* **619**, 572 (2015).
- ³M. Higashiwaki, K. Sasaki, H. Murakami, Y. Kumagai, A. Koukitu, A. Kuramata, T. Masui, and S. Yamakoshi, *Semicond. Sci. Technol.* **31**, 034001 (2016).
- ⁴M. Baldini, Z. Galazka, and G. Wagner, *Mater. Sci. Semicond. Process.* **78**, 132 (2018).
- ⁵A. J. Green, K. D. Chabak, M. Baldini, N. Moser, R. Gilbert, R. C. Fitch, G. Wagner, Z. Galazka, J. McCandless, A. Crespo, K. Leedy, and G. H. Jessen, *IEEE Electron Device Lett.* **38**, 790 (2017).
- ⁶Z. Galazka, R. Uecker, K. Irmscher, M. Albrecht, D. Klimm, M. Pietsch, M. Brützm, R. Bertram, S. Ganschow, and R. Fornari, *Cryst. Res. Technol.* **45**, 1229 (2010).
- ⁷H. Aida, K. Nishiguchi, H. Takeda, N. Aota, K. Sunakawa, and Y. Yaguchi, *Jpn. J. Appl. Phys., Part I* **47**, 8506 (2008).
- ⁸Z. Galazka, R. Uecker, D. Klimm, K. Irmscher, M. Naumann, M. Pietsch, A. Kwasniewski, R. Bertram, S. Ganschow, and M. Bickermann, *ECS J. Solid State Sci. Technol.* **6**, Q3007 (2017).
- ⁹A. Kuramata, K. Koshi, S. Watanabe, Y. Yamaoka, T. Masui, and S. Yamakoshi, *Jpn. J. Appl. Phys., Part II* **55**, 1202A2 (2016).
- ¹⁰G. Wagner, M. Baldini, D. Gogova, M. Schmidbauer, R. Schewski, M. Albrecht, Z. Galazka, D. Klimm, and R. Fornari, *Phys. Status Solidi A* **211**, 27 (2014).
- ¹¹M. Baldini, M. Albrecht, A. Fiedler, K. Irmscher, D. Klimm, R. Schewski, and G. Wagner, *J. Mater. Sci.* **51**, 3650 (2016).
- ¹²M. Baldini, M. Albrecht, A. Fiedler, K. Irmscher, R. Schewski, and G. Wagner, *ECS J. Solid State Sci. Technol.* **6**, Q3040 (2017).
- ¹³T. Oshima, N. Arai, N. Suzuki, S. Ohira, and S. Fujita, *Thin Solid Films* **516**, 5768 (2008).
- ¹⁴M.-Y. Tsai, O. Bierwagen, M. E. White, and J. S. Speck, *J. Vac. Sci. Technol., A* **28**, 354 (2010).
- ¹⁵K. Sasaki, M. Higashiwaki, A. Kuramata, T. Masui, and S. Yamakoshi, *J. Cryst. Growth* **378**, 591 (2013).
- ¹⁶K. Nomura, K. Goto, R. Togashi, H. Murakami, Y. Kumagai, A. Kuramata, S. Yamakoshi, and A. Koukitu, *J. Cryst. Growth* **405**, 19 (2014).
- ¹⁷H. Murakami, K. Nomura, K. Goto, K. Sasaki, K. Kawara, Q. T. Thieu, R. Togashi, Y. Kumagai, M. Higashiwaki, A. Kuramata, S. Yamakoshi, B. Monemar, and A. Koukitu, *Appl. Phys. Express* **8**, 015503 (2015).
- ¹⁸M. Higashiwaki, H. Murakami, Y. Kumagai, and A. Kuramata, *Jpn. J. Appl. Phys., Part II* **55**, 1202A1 (2016).
- ¹⁹R. Schewski, M. Baldini, K. Irmscher, A. Fiedler, T. Markurt, B. Neuschulz, T. Remmele, T. Schulz, G. Wagner, Z. Galazka, and M. Albrecht, *J. Appl. Phys.* **120**, 225308 (2016).
- ²⁰A. Fiedler, R. Schewski, M. Baldini, Z. Galazka, G. Wagner, M. Albrecht, and K. Irmscher, *J. Appl. Phys.* **122**, 165701 (2017).
- ²¹S. Rafique, L. Han, A. T. Neal, S. Mou, J. Boeckl, and H. Zhao, *Phys. Status Solidi A* **215**, 1700467 (2017).
- ²²P. Mazzolini, P. Vogt, R. Schewski, C. Wouters, M. Albrecht, and O. Bierwagen, *APL Mater.* **7**, 022511 (2019).
- ²³K. Sasaki, A. Kuramata, T. Masui, E. G. Villora, K. Shimamura, and S. Yamakoshi, *Appl. Phys. Express* **5**, 035502 (2012).
- ²⁴K. Irmscher, Z. Galazka, M. Pietsch, R. Uecker, and R. Fornari, *J. Appl. Phys.* **110**, 123511 (2011).
- ²⁵Z. Galazka, K. Irmscher, R. Uecker, R. Bertram, M. Pietsch, A. Kwasniewski, M. Naumann, T. Schulz, R. Schewski, D. Klimm, and M. Bickermann, *J. Cryst. Growth* **404**, 184 (2014).
- ²⁶V. Blum, R. Gehrke, F. Hanke, P. Havu, V. Havu, X. Ren, K. Reuter, and M. Scheffler, *Comput. Phys. Commun.* **180**, 2175 (2009).
- ²⁷V. Havu, V. Blum, P. Havu, and M. Scheffler, *J. Comput. Phys.* **228**, 8367 (2009).
- ²⁸J. P. Perdew, A. Ruzsinszky, G. I. Csonka, O. A. Vydrov, G. E. Scuseria, L. A. Constantin, X. Zhou, and K. Burke, *Phys. Rev. Lett.* **100**, 136406 (2008).
- ²⁹A. V. Krukau, O. A. Vydrov, A. F. Izmaylov, and G. E. Scuseria, *J. Chem. Phys.* **125**, 224106 (2006).
- ³⁰S. P. Ong, W. D. Richards, A. Jain, G. Hautier, M. Kocher, S. Cholia, D. Gunter, V. L. Chevrier, K. A. Persson, and G. Ceder, *Comput. Mater. Sci.* **68**, 314 (2013).
- ³¹R. Tran, Z. Xu, B. Radhakrishnan, D. Winston, W. Sun, K. A. Persson, and S. P. Ong, *Sci. Data* **3**, 160080 (2016).
- ³²W. Sun and G. Ceder, *Surf. Sci.* **617**, 53 (2013).
- ³³V. M. Bermudez, *Chem. Phys.* **323**, 193 (2006).
- ³⁴D. J. Chadi, *Phys. Rev. Lett.* **59**, 1691 (1987).
- ³⁵G. R. Bell, T. S. Jones, and B. A. Joyce, *Surf. Sci.* **429**, L492 (1999).
- ³⁶S.-H. Han, A. Mauze, E. Ahmadi, T. Mates, Y. Oshima, and J. S. Speck, *Semicond. Sci. Technol.* **33**, 045001 (2018).